




# Impact of annealing temperature on structural, optical, and Mössbauer properties of nanocrystalline NiFe<sub>2</sub>O<sub>4</sub>

H. S. Mund<sup>1,\*</sup> , Pradeep Prajapat<sup>2</sup>, Saroj Dhaka<sup>3</sup>, Sudesh Kumar<sup>3</sup>, Abhishek Saxena<sup>2</sup>, and Sher Singh Meena<sup>4,\*</sup>

<sup>1</sup>Department of Physics, K. R. College (J P University, Chapra), Gopalganj, Bihar 841428, India

<sup>2</sup>Pacific Academy of Higher Education and Research University, Udaipur, Rajasthan 313001, India

<sup>3</sup>Department of Chemistry, Banasthali University, Banasthali, Rajasthan 304022, India

<sup>4</sup>Solid State Physics Division, Bhabha Atomic Research Centre, Mumbai 400085, India

Received: 19 July 2021

Accepted: 21 September 2021

Published online:

28 September 2021

© The Author(s), under exclusive licence to Springer Science+Business Media, LLC, part of Springer Nature 2021

## ABSTRACT

In this paper, we have investigated the effect of annealing temperature on the structural, optical, and Mössbauer properties of nanocrystalline (NC) nickel ferrites (NFOs) synthesized by the sol-gel auto-combustion method. The NFOs were characterized by X-Ray diffraction (XRD), Raman spectroscopy, Diffusion reflectance spectroscopy (DRS), and Mössbauer spectroscopy techniques. The XRD results show that the average crystallite size increases from 27.5 to 54.3 nm when increasing the annealing temperature from 200 to 1000 °C. The Ultraviolet-Visible Diffuse Reflectance Spectroscopy (UV-DRS) measurement is used to find the optical band gap observed between 1.92 and 1.75 eV for NFOs annealed at 200 and 1000 °C, respectively. The Mössbauer study confirmed that the structure transforms from mixed spinel to inverse spinel structure when moving to higher annealing temperature.

## 1 Introduction

During the last few decades, nanocrystalline (NC) spinel ferrites having structural formula  $A\text{Fe}_2\text{O}_4$  (where  $A = \text{Mn, Fe, Co, Ni, Zn, Mg, etc.}$ ) are the most studied material due to their wide technological and medical applications like the microwave devices, magnetic memory devices, drug delivery, recording media, gas sensors, biosensors, photo-catalysis, magnetic resonance, electrodes, converters, ferroelectric devices, magnetic disks, phase shifters, etc.

[1–19]. Among all the spinel ferrites, nickel ferrites (NFOs) have been investigated widely due to their peculiar properties like high chemical stability, catalytic behavior, ferromagnetic behavior, high resistivity, and low coercivity [2–7, 13–18]. Nickel ferrites have an inverse spinel structure with space group  $Fd\bar{3}m$  where  $\text{Fe}^{3+}$  ions are equally distributed in between the octahedral and tetrahedral site and  $\text{Ni}^{2+}$  ion occupies an octahedral site which may be represented as  $(\text{Fe}^{3+})_T(\text{Ni}^{2+}\text{Fe}^{3+})_O\text{O}^{2-}_4$  [3, 5, 7, 14]. In recent years, several methods have been employed to synthesize nanocrystalline or nanoparticle NFOs like

Address correspondence to E-mail: hmoond@gmail.com; ssingh@barc.gov.in

hydrothermal, sol–gel, solid-state reaction, chemical co-precipitation, plasma deposition, high-energy ball milling, microwave processing, etc. [9–17]. Among these methods, the sol–gel auto-combustion method is an excellent technique to synthesize low-cost, high-purity, homogeneous, and ultrafine nanoparticle powder. It is well known that the factors that affect the physical and chemical properties of nanocrystalline ferrites are the synthesis procedure, cation distribution, annealing temperature, surface spin, etc.

The electrochemical performance of Ni-ferrite as a supercapacitor electrode has been evaluated by Patil et al. and their utility for energy storage applications is highlighted [2]. Wang et al. have studied the photocatalytic activities of NiFe<sub>2</sub>O<sub>4</sub> 3D nanosphere prepared by Glycerol-assisted microwave solvothermal method [4]. The authors found that the 3D NFO has a high degradation ability which can rapidly degrade organic pollutants. The magnetic and biological properties of NiFe<sub>2</sub>O<sub>4</sub> nanoparticles prepared by the polymeric precursor method have been evaluated by Santos et al. [5]. They explore the possibility of S-NiFe<sub>2</sub>O<sub>4</sub> nanoparticles as drug delivery agents in targeted cancer therapy. Pottker et al. [7] have investigated the effect of structural order–disorder on the optical and magnetic properties of NiFe<sub>2</sub>O<sub>4</sub> nanoparticles synthesized by the co-precipitation method and calcined in the ambient atmosphere at 700, 800, 900, and 1000 °C temperatures. The synthesis of porous NiFe<sub>2</sub>O<sub>4</sub> microspheres by the one-step solvothermal method has been reported by Zhang et al. [16]. The authors show that NiFe<sub>2</sub>O<sub>4</sub> microspheres have promising applications as high-performance acetone gas sensors. Majid et al. have investigated the magnetic, structural, and dielectric properties of NiFe<sub>2</sub>O<sub>4</sub> prepared by hydrothermal and sol–gel routes [20]. The results show that the synthesis method affects NiFe<sub>2</sub>O<sub>4</sub> properties; therefore, a suitable method can be used for the desired properties. Baig et al. have synthesized NiFe<sub>2</sub>O<sub>4</sub>/SiO<sub>2</sub> nanostructure material for high-rated supercapacitors electrode [21]. Mandal et al. [22, 23] have detailed morphology studies on NiFe<sub>2</sub>O<sub>4</sub> to enhance their microwave applications. Nanocrystalline NiFe<sub>2</sub>O<sub>4</sub> is a soft material with low coercivity and saturation magnetization. Senthilkumar et al. have synthesized sub-microns size NiFe<sub>2</sub>O<sub>4</sub> particles by the molten salt technique at 900 °C with different weight ratios of NaCl:KCl. The values of saturation magnetization ( $M_s$ ) were found to be increased from 31.58 to

44.19 emu/g, whereas the value of coercivity ( $H_C$ ) was decreased from 246.7 to 86.7 Oe with increasing the NaCl:KCl ratio from 4:0 to 0:4 [24]. Gao et al. have studied metal–organic frameworks (MOFs)-derived magnetic porous carbon microspheres constructed by core–shell Ni@C structure and found similar magnetic properties like NiFe<sub>2</sub>O<sub>4</sub> nanoparticles [25]. The values of  $M_s$  and  $H_C$  were found between 21–25 emu/g and 19.5–26.3 Oe, respectively [25].

In the present study, nanocrystalline nickel ferrites were synthesized by the sol–gel method following different annealing temperatures. The structural, optical, and Mössbauer properties of annealed nanocrystalline nickel ferrites were evaluated and correlated with crystallite size, lattice parameter, etc. The Mössbauer spectroscopy measurements assessed the effect of annealing temperature on the cations distribution.

## 2 Experimental work

Nanocrystalline (NC) nickel ferrites (NFOs) were prepared by the sol–gel method using SRL high-purity nickel nitrate (purity  $\geq 99\%$ ) and ferric nitrate (purity  $\geq 98\%$ ), and citric acid (purity  $\geq 99.7\%$ ) as starting material and fuel, respectively. The raw material for NFOs was prepared by dissolving stoichiometric amounts of the metal nitrates and citric acid in the same molar ratio (1:1). The raw materials solution was stirred at 50 °C for half an hour using a magnetic agitator with a hot plate. After that, the temperature was raised to 100 °C to get the gel form of a solution which produces powder of NFOs by achieving the auto-combustion. This powder was ground in an agate mortar and then annealed at different temperatures i.e., 200 (hereafter referred to as NFO-01), 400 (referred as NFO-02), 600 (referred as NFO-03), 800 (referred as NFO-04), and 1000 °C (referred as NFO-05) for 6 h.

The crystal structure of annealed NFOs was confirmed by using Cu-K $\alpha$  lines (wavelength  $\lambda = 1.540 \text{ \AA}$ ) of Rigaku Ultima IV X-Ray diffractometer (XRD) with a step size of 0.02° in the 2 $\theta$  range between 20 and 70°. The Confocal Raman spectrometer (STR-500) with 5 mW optimized laser power of 532 nm DPSS laser was carried out to study the electronic properties of annealed NFOs. The optical properties of annealed NFOs were carried out using UV–Vis DRS spectroscopy measurement in the

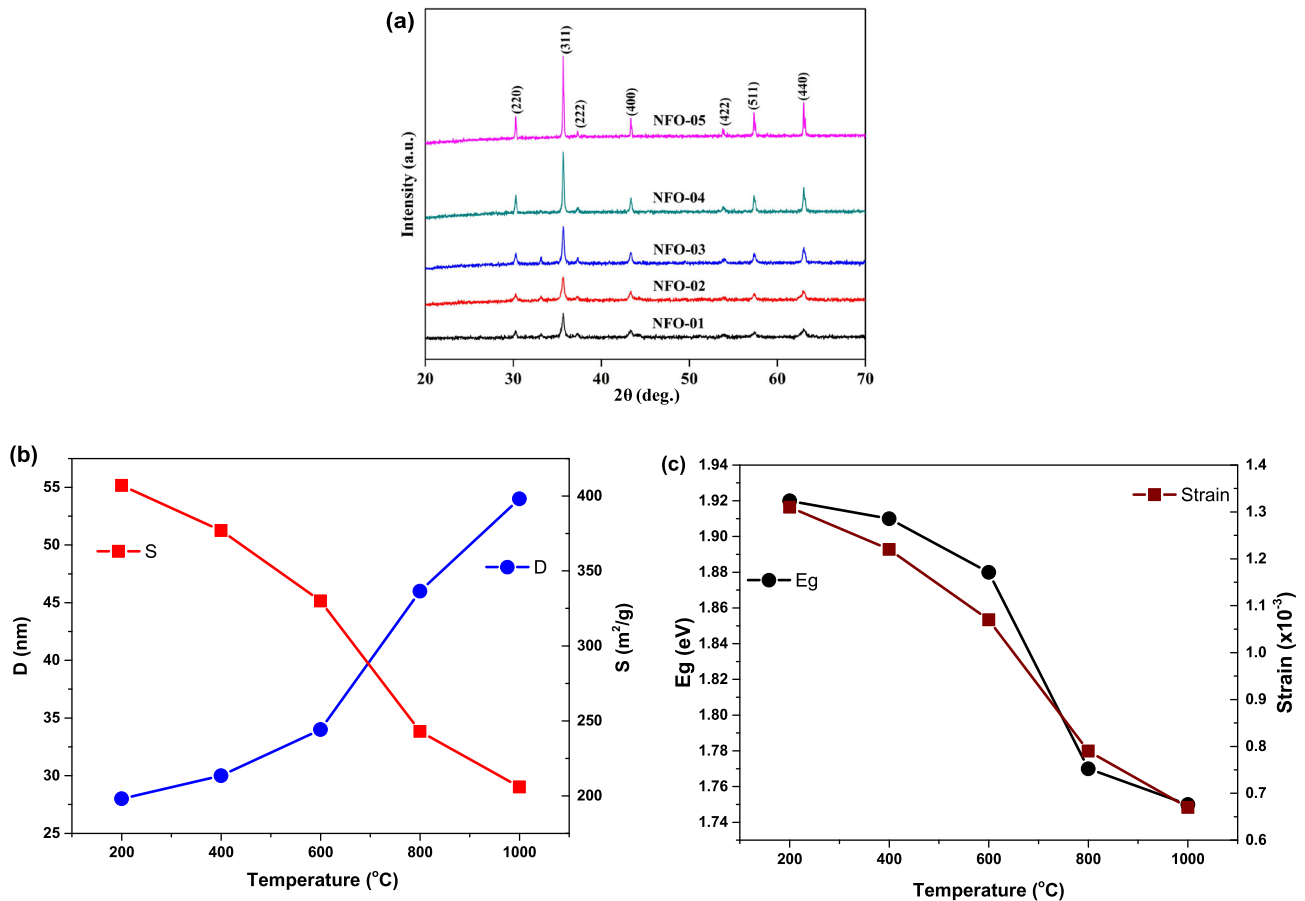


**Fig. 1** a X-ray diffraction pattern of nanocrystalline Ni-ferrite annealed at different temperature i.e., 200 (NFO-01), 400 (NFO-02), 600 (NFO-03), 800 (NFO-04), and 1000 °C (NFO-05).

b Variation in crystallite size (D) and surface area (S) with increasing the annealing temperature. c Variation in strain ( $\zeta$ ) with band gap energy ( $E_g$ ) with increasing the annealing temperature

**Table 1** Structural parameters like lattice parameter (a), crystallite size (D), surface area (S), dislocation density ( $\delta$ ), strain ( $\zeta$ ), and band gap energy ( $E_g$ ) of nanocrystalline NFOs annealed at different temperature

Parameters	Sample (annealing temperature in °C)				
	NFO-01 (200)	NFO-02 (400)	NFO-03 (600)	NFO-04 (800)	NFO-05 (1000)
a (Å)	8.345	8.346	8.341	8.339	8.340
D (nm)	28	30	34	46	54
$I_{220}/I_{222}$	1.67	1.908	1.786	3.563	3.926
$I_{420}/I_{222}$	0.72	0.89	1.593	1.098	1.367
$\delta \times 10^{15}$ (m <sup>-2</sup> )	1.32	1.14	0.87	0.47	0.34
$\zeta \times 10^{-3}$	1.31	1.22	1.07	0.79	0.67
$E_g$ (eV)	1.92	1.91	1.88	1.77	1.75

wavelength range 200–800 nm. The room temperature Mössbauer spectra of NFOs were recorded in transmission geometry using a constant acceleration mode Mössbauer spectrometer with <sup>57</sup>Co source in

Rh matrix of 5 mCi strength. High-purity <sup>57</sup>Fe metal foil was used for velocity calibration. The Win-Normos site fitting program was performed to fit all the Mössbauer spectra.

**Fig. 2** Raman spectra of nanocrystalline Ni-ferrite

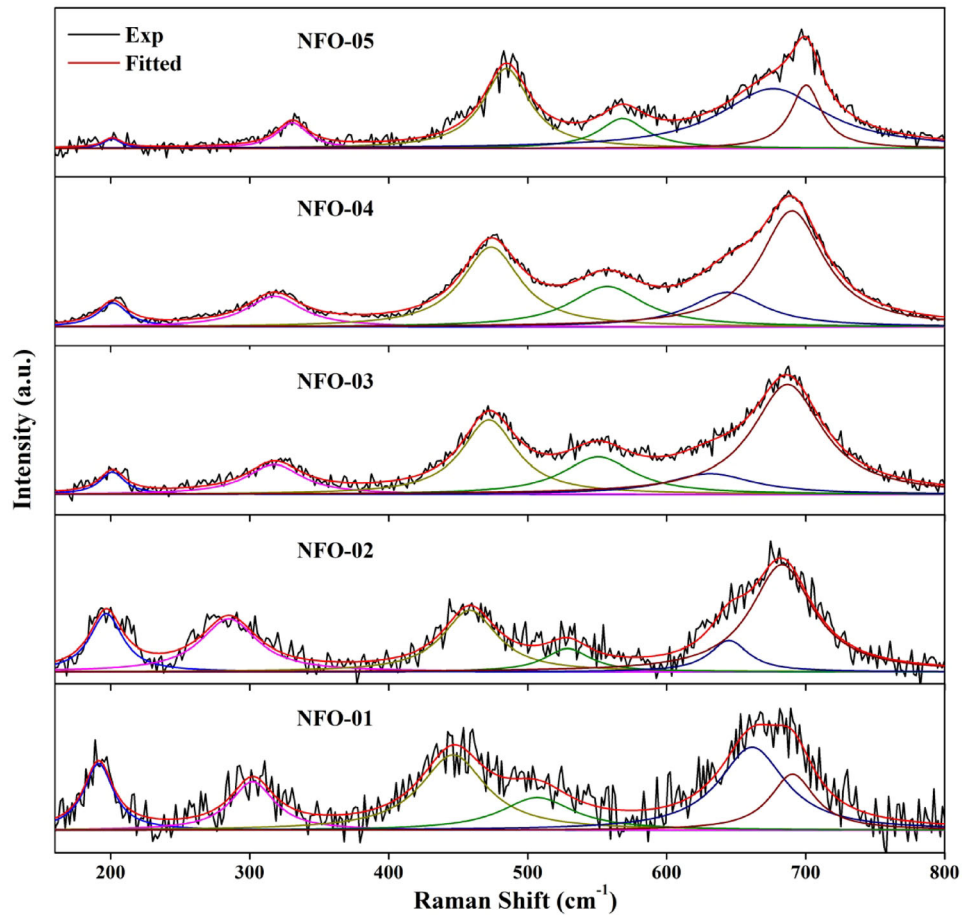


**Table 2** Raman modes of nanocrystalline NFOs annealed at different temperature

Sample (annealing temperature in °C)	Raman modes (cm <sup>-1</sup> )				
	T <sub>2g</sub> (1)	E <sub>g</sub>	T <sub>2g</sub> (2)	T <sub>2g</sub> (3)	A <sub>1g</sub> (1)
NFO-01 (200)	188	310	453	543	674
NFO-02 (400)	194	303	459	554	674
NFO-03 (600)	203	322	471	557	687
NFO-04 (800)	207	323	477	557	687
NFO-05 (1000)	207	332	481	567	697

### 3 Results and discussion

The XRD patterns for nanocrystalline NFOs synthesized via the sol-gel method and annealed at a different temperature from 200 to 1000 °C are shown in Fig. 1a. The intensity peaks of the XRD pattern confirm the formation of the single phase cubical spinel structure of nickel ferrite with space group *Fd3m*, which is in good agreement with the JCPDS card 74-2081. The crystallite size (*D*) was calculated using the Debye-Scherrer formula as in the following equation [26, 27]:

$$D = 0.94\lambda / \beta \cdot \cos \theta \tag{1}$$

where  $\lambda$  the wavelength of X-Ray and  $\beta$  is broadening of the peak (311) at a diffraction angle ( $\theta$ ), while the theoretical X-Ray density ( $d_x$ ) and dislocation density ( $\delta$ ) were calculated using the following equations [27]:

$$d_x = 8M / N_A \cdot a^3 \tag{2}$$

$$\delta = 1 / D^2 \tag{3}$$

where  $M$  is the compound's molecular weight and  $N_A$  and  $a$  are Avogadro's number and the lattice

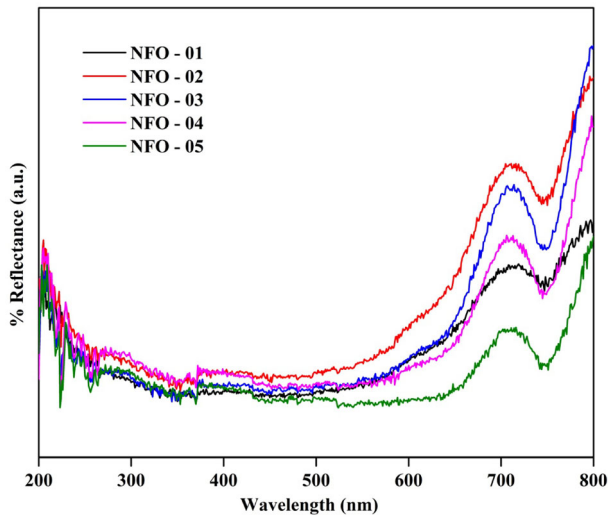


**Fig. 3** UV-DRS diffuse reflectance spectra of nanocrystalline Ni ferrites

parameter, respectively. The crystallite size calculated using the most intense peak and the lattice constant, density, and strain are tabulated in Table 1. The XRD result confirms the formation of nanocrystalline material. The XRD results show that the crystallinity increases with the annealing temperature as the intensity of the most intense diffraction peak increases and peak width decrease with increasing annealing temperature which shows an enhancement in the phase crystallinity of annealed NFOs [28–36]. The crystallite size increases from ~ 28 to 54 nm with an increase in annealing temperature from 200 to 1000 °C, respectively, while strain decreases with an increase in annealing temperature (Fig. 1b, c). Almessiere et al. have studied  $[\text{Ni}_{0.4}\text{Cu}_{0.2}\text{Zn}_{0.4}](\text{Fe}_{2-x}\text{Tb}_x)\text{O}_4$  ( $x \leq 0.1$ ) nanospinel ferrites and found the crystallite size to be increased from 12 to 19 nm, whereas there is no such trend in the average particle size and it fluctuated between 19 and 70 nm [37]. The small particles combined to form larger grain boundaries under the re-crystallization process (reduce interparticle distance) as increasing annealing temperature decreases the lattice strain and defects (indicates an improvement in the crystallinity). The slight variation in lattice parameters with increasing annealing temperature may be due to ordering in unit cells. The present pattern/trend of XRD results are in good agreement with the earlier reported data [28, 29].

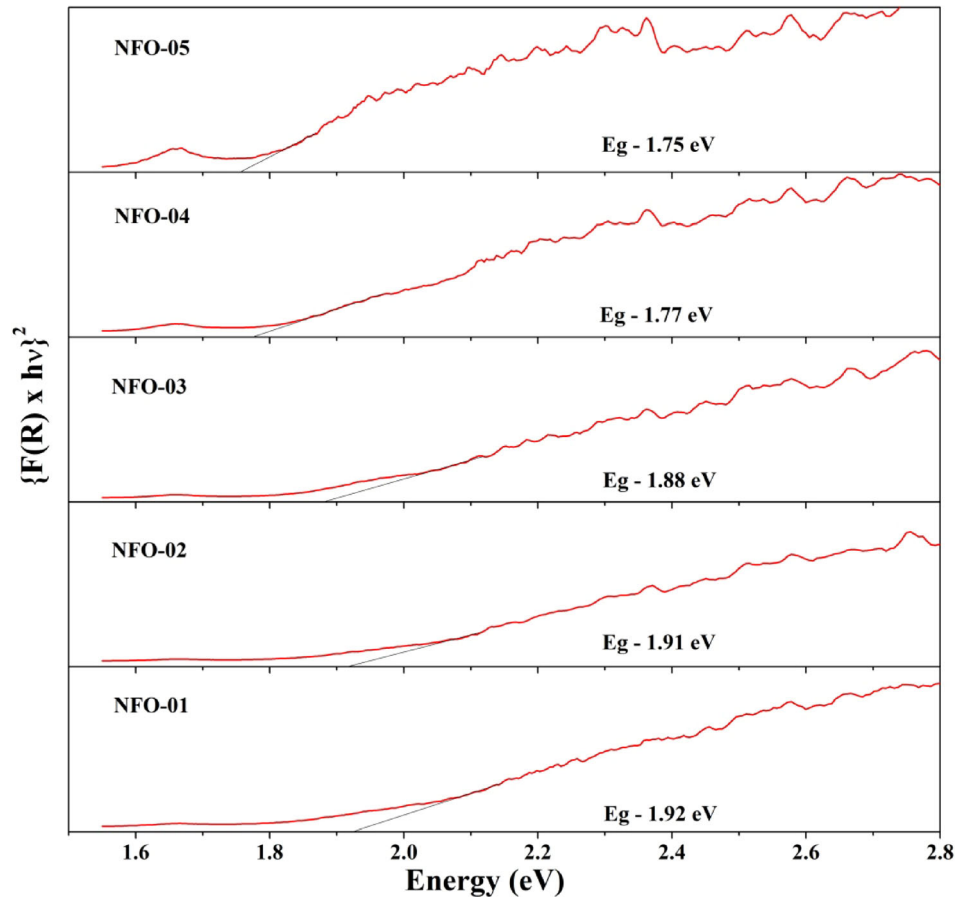
In mostly cubic spinel ferrites XRD data, the peaks (220) and (422) belong to tetrahedral sites (8a), while

the peak at (222) belongs to octahedral sites (16d) and we can get the cationic distribution ratio by using these peaks intensity or area. Thus, the ratios  $I_{220}/I_{222}$  and  $I_{422}/I_{222}$  are an indication of the A- and B-sites occupation. The experimental relative intensities  $I_{220}/I_{222}$  and  $I_{422}/I_{222}$  of  $\text{NiFe}_2\text{O}_4$  as a function of annealing temperature are given in Table 1. The observed values ( $I_{220}/I_{222}$ ) lie between 1.67 and 3.93, and show an increase with the sintering temperature. The observed values of  $I_{220}/I_{222}$  are compatible with the reported values (0.8–3.6) [38]. The increase in the  $I_{220}/I_{222}$  ratio with annealing temperature indicates that the cation concentration in the A-site increases when compared to that of the B-site, this suggests the formation of a inverse spinel structure from a mixed spinel structure.

The room temperature Raman spectroscopy measurement has been carried out to interpret vibrational and structural properties of nanocrystalline NFOs [28–31, 39]. The Lorentzian line shape least square-fitted Raman spectra of NFOs in the range of 160–800  $\text{cm}^{-1}$  are shown in Fig. 2. The five or more active Raman modes in the Factor group analysis confirm the spinel structure formation of NFOs [28, 29]. The measured Raman modes of NFOs are tabulated in Table 2. Earlier reports on Raman spectroscopy analysis of spinel ferrites show that Raman modes in the region 660–720  $\text{cm}^{-1}$  and 460–640  $\text{cm}^{-1}$  explored the nature of the tetrahedral and octahedral sites [28–31]. The symmetric stretching vibrations of the Metal (M)—Oxygen (O) bond at the tetrahedral site creates  $A_{1g}$  mode, while  $E_g$  mode is produced by the symmetric bending of the M–O bond. The  $T_{2g}(2)$  and  $T_{2g}(3)$  modes are due to the asymmetric stretching of M–O ions and bending of oxygen ion, respectively, at the octahedral site, while the translation movement of the metal ion together with four oxygen atoms at the tetrahedral site attribute to  $T_{2g}(1)$  mode. A double-peak-like structure of  $A_{1g}$  mode (splitting of  $A_{1g}$  mode into doublet like peak) in all NFOs may be due to the distribution of Fe/Ni–O bond length (as ionic radii of Fe and Ni ions are different), where one peak corresponds to the Fe–O bond and the other one is due to the mixing of Fe and Ni ions band with oxygen. Thus, Raman spectroscopy analysis confirms the formation of mixed spinel structure of NFOs. The present result shows that Raman mode shifts toward high wavenumber as increasing the annealing temperature, indicating that mixed spinel structure



**Fig. 4** Optical band gap energy determination of nanocrystalline Ni ferrites by plot of  $\{F(R) \times hv\}^2$  vs energy ( $hv$ )



moves toward the inverse spinel structure with increasing the annealing temperature.

To understand the influence of annealing temperature on the optical properties of the nanocrystalline NFOs, the Ultraviolet–Visible Diffuse Reflectance Spectroscopy (UV–Vis DRS) measurement has been performed. The UV–Vis DRS results are shown in Fig. 3, which shows a significant change in absorbance spectra with the annealing temperature. The spectroscopy data were analyzed using the Kubelka Munk function using the reflectance and absorption data such as follows [6, 39–44]:

$$F(R) = \alpha = \left\{ (1 - R)^2 / 2R \right\} \tag{4}$$

where  $F(R)$  is the Kubelka–Munk function,  $\alpha$  is the absorption coefficient, and  $R$  is the reflection coefficient. The energy bandgap of all the NC NFOs is calculated using the Tauc equations such as the following [6, 43, 44]:

$$(\alpha hv)^n = A(hv - E_g) \tag{5}$$

where  $hv$ ,  $n$ ,  $E_g$ , and  $A$  are photon energy, index of the optical transition, bandgap energy, and constant depending on the material, respectively. The index ( $n$ ) value could be 2 or 1/2 depending on the direct or indirect optical transition, respectively. Figure 4 shows the energy bandgap for all annealed NC NFOs. Our results show that the bandgap of NFO-05 (1.75 eV) is narrower than that of NFO-01 (1.92 eV). The estimated band values of NFO-01, NFO-02, NFO-03, NFO-04, and NFO-05 were 1.92, 1.85, 1.81, 1.75, and 1.75 eV, respectively. This shows that the energy band of nanocrystalline NFOs has shifted toward the lower energy side (redshift) with increasing the annealing temperature. It is found that the energy bandgap value can be affected by various factors like annealing temperature, preparation method, doping, crystallite size, etc. [39–45]. Researchers have reported that the band gap energy decreases with an increase in annealing temperature [41, 46]. The decrease in bandgap values with increasing annealing temperature may be due to the grain growth (recrystallization process) and the presence of the

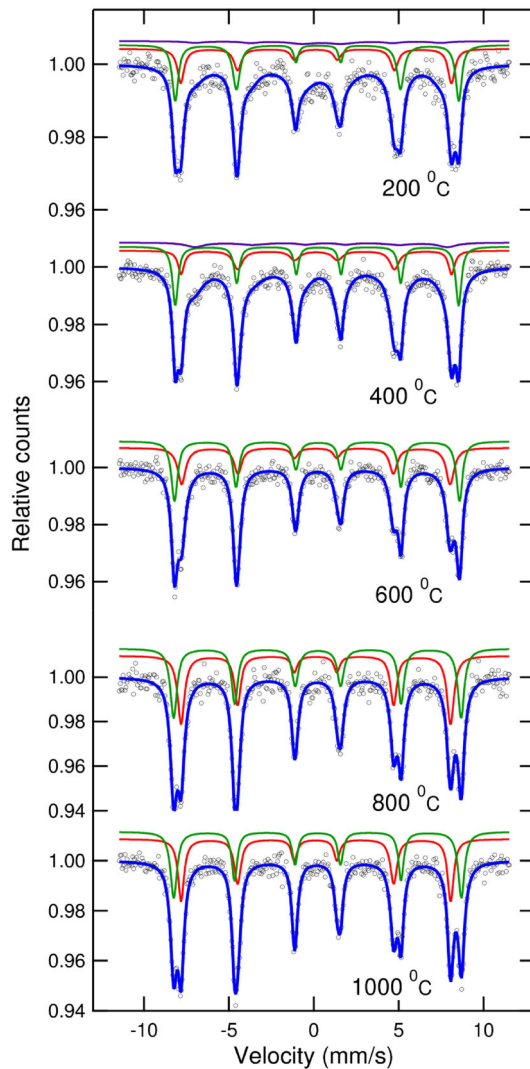


**Fig. 5** Room temperature Mössbauer spectra of NiFe<sub>2</sub>O<sub>4</sub> spinel ferrites synthesized heated at various temperatures

defects. Our result also shows similar behavior for annealed nanocrystalline NFOs.

Mössbauer spectra for annealed nanocrystalline NFOs were recorded at room temperature using a Mössbauer spectrometer operated in constant acceleration mode (triangular wave) in transmission geometry shown in Fig. 5 and the analysis results are given in the Table S1. The Mössbauer spectra of NFO-01 and NFO-02 are fitted with three sextets, whereas Mössbauer spectra of NFO-03, NFO-04, and NFO-05 are fitted with two sextets. The two sextets are originated due to the tetrahedral and octahedral environment of Fe ions, while the third sextet (with less hyperfine field area) in NFO-01 and NFO-02 may be due to the canted Fe<sup>3+</sup> spin ions due to comparatively

small particles [18, 34, 36, 47, 48]. The various hyperfine interaction parameters like isomer shift ( $\delta$ ), quadrupole splitting ( $\Delta$ ) magnetic hyperfine field ( $H_f$ ), relative area ( $R_A$ ), outer line width of sextets ( $\Gamma$ ), and average outer line width of sextets ( $\langle \Gamma \rangle$ ) obtained from Mössbauer spectra and the variation in these parameters with annealing temperature are shown in Fig. 6a–e, respectively. Earlier studies show that the room temperature Mössbauer spectra of NFOs nanocrystalline are typically a superposition of quadrupole doublet and magnetic sextets [18, 48]. In contrast, in the present study, we have observed only sextets. Our results show that the intensity of sextet's increases and the average values of outer line width ( $\langle \Gamma \rangle$ ) absorption spectra become sharper with increasing the annealing temperature (Fig. 6e). This sharpness is due to the increasing crystallite size and distribution of Ni<sup>2+</sup> and Fe<sup>3+</sup> ions at B-site creating a hyperfine field at A-site. The isomer shift ( $\delta$ ) for octahedral Fe<sup>3+</sup> ions (sextet B) is more than that for the tetrahedral Fe<sup>3+</sup> ions which shows that Fe<sup>3+</sup> ions are more covalent at the tetrahedral site [49–52].

The value of isomer shift of Fe<sup>3+</sup> ions at A- and B-sites remains nearly constant as increasing annealing temperature which shows a small migration of Ni ions from A-site to B-site (Fig. 6a). The values of isomer shift for the tetrahedral site are found between  $\delta = 0.23$ – $0.26$  mm/s and for the octahedral site they are found between  $\delta = 0.34$ – $0.68$  mm/s with respect to  $\alpha$ -Fe ( $\delta = 0.0$  mm/s) foil. The range of isomer shift values indicates Fe ions are in Fe<sup>3+</sup> valence state with high spin state configuration [53–56].

The magnetic hyperfine field of the A-site is less than that of the B-site may be due to the covalent nature of the tetrahedral site. The relative area ratio under the resonance curve of Mössbauer spectra is used to determine the Fe sites occupancy and cations distribution in the prepared samples [48, 57]. Cation distribution derived from Mössbauer study of nanocrystalline NFOs heated at different temperatures is shown in Table 3. Our result indicates that the Ni concentration at B-site increases as increasing annealing temperature. This demonstrates that nanocrystalline NFOs structure transforms from mixed spinel to inverse spinel structure when moving to higher annealing temperature. The sample annealed at 1000 °C is showing a pure inverse spinel structure. Thus Mössbauer study supports Raman spectra results.

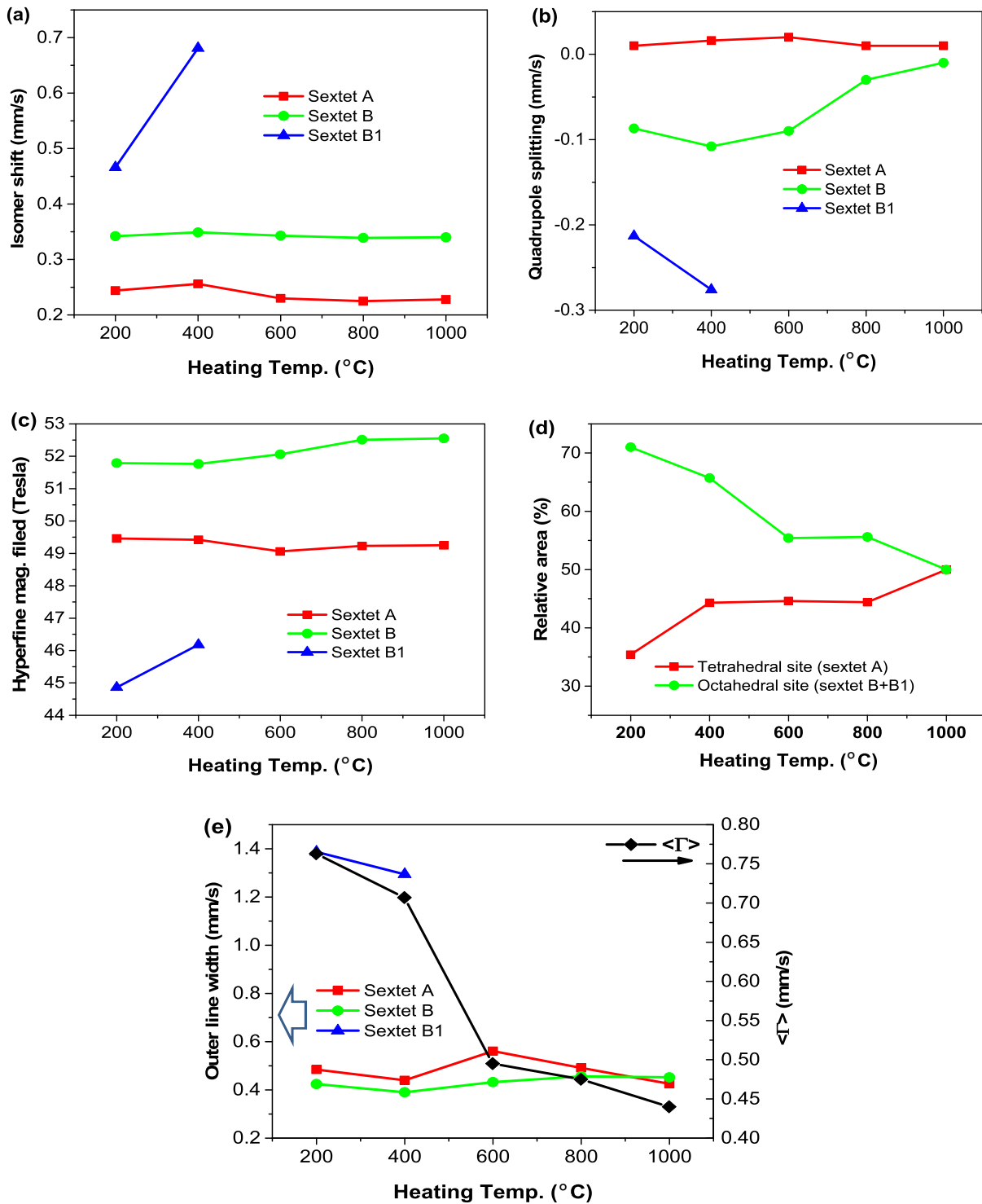


**Fig. 6** Variation in different Mossbauer parameters with sintering temperature; **a** isomer shift, **b** quadrupole splitting, **c** hyperfine field ( $H_f$ ), **d** relative area of tetrahedral and octahedral sites, and

**e** outer line width of each sites and the average value of outer line width ( $\langle \Gamma \rangle$ )



**Table 3** Cation distribution derived from Mössbauer study of NiFe<sub>2</sub>O<sub>4</sub>-NPs heated at different temperatures. Brackets ( )<sub>A</sub> and [ ]<sub>B</sub> represent the tetrahedral and octahedral sites, respectively

Annealing Temp. (°C)	Fe ions at A-site (%)	Fe ions at B-site (%)	Cation distribution
200	35.4	64.6	(Fe <sub>0.58</sub> Ni <sub>0.42</sub> ) <sub>A</sub> [Fe <sub>1.42</sub> Ni <sub>0.58</sub> ] <sub>B</sub> O <sub>4</sub>
400	44.3	55.7	(Fe <sub>0.686</sub> Ni <sub>0.314</sub> ) <sub>A</sub> [Fe <sub>1.314</sub> Ni <sub>0.686</sub> ] <sub>B</sub> O <sub>4</sub>
600	44.6	55.4	(Fe <sub>0.892</sub> Ni <sub>0.108</sub> ) <sub>A</sub> [Fe <sub>1.108</sub> Ni <sub>0.892</sub> ] <sub>B</sub> O <sub>4</sub>
800	44.4	55.6	(Fe <sub>0.888</sub> Ni <sub>0.112</sub> ) <sub>A</sub> [Fe <sub>1.112</sub> Ni <sub>0.888</sub> ] <sub>B</sub> O <sub>4</sub>
1000	50.0	50.0	(Fe) <sub>A</sub> [FeNi] <sub>B</sub> O <sub>4</sub>

## 4 Conclusions

The influence of annealing temperature on the structural, optical, and Mössbauer properties of nanocrystalline NFOs synthesized via the sol–gel method has been investigated in this study. The XRD results revealed that the value of crystallite size increases from 28 to 54 nm with increase in annealing temperature. The Raman spectra of nanocrystalline NFOs confirm the formation of spinel structure with five Raman active modes. The Raman mode shifts toward high wavenumber as increasing the annealing temperature indicates that mixed spinel structure moves toward the inverse spinel structure with increasing the annealing temperature. Using UV-DRS spectra, the optical bandgap energy of nanocrystalline NFOs was calculated between ranges 1.75 to 1.92 eV. Results show that the energy band shifted toward the lower energy side (redshift) to increase the annealing temperature. In Mössbauer spectra, the value of isomer shift of Fe<sup>3+</sup> ions at sites A and B remains nearly constant with increasing annealing temperature, which shows a minimal migration of Ni ions from A-site to B-site which indicates structure transformation from mixed spinel to inverse spinel as increasing annealing temperature.

## Acknowledgements

The authors are thankful to the Head, Department of Physics M.L. Sukhadia University, Udaipur for providing XRD facility and MRC, MNIT Jaipur for Raman spectroscopy measurements and also grateful to Prof. L. K. Kennedy Department of Physics, VIT Chennai for providing DRS facility. One of us (HSM) is grateful to Science and Engineering Research Board (SERB), New Delhi for proving grant under Core Research Grant Scheme (CRG/2020/002826). The

authors are thankful to Dr. Vidyadhar Singh, Dept. of Physics, J P University, Chapra for his support during the revision.

## Declarations

**Conflict of interest** The authors declare that they have no conflict of interest.

**Supplementary Information:** The online version contains supplementary material available at <http://doi.org/10.1007/s10854-021-07089-6>.

## References

1. T.V. Sagar, T.S. Rao, K.C.B. Naidu, *Ceram. Int.* **46**, 11515 (2020)
2. P.D. Patil, S.R. Shingte, V.C. Karade, J.H. Kim, T.D. Dongale, S.H. Mujawar, A.M. Patil, P.B. Patil, *J. Energy Storage* **40**, 102821 (2021)
3. D.K. Dinkar, B. Das, R. Gopalan, B.S. Dehiya, *Mater. Chem. Phys.* **218**, 70 (2018)
4. Y. Wang, H. Wang, Y. Yang, B. Xin, *Ceram. Int.* **47**, 14594 (2021)
5. J.G. Santos, H. Lopes, H. Moreno, M.A. Ramirez, F.G. Garcia, A.Z. Simoes, *Ceram. Int.* **47**, 16152 (2021)
6. K. Kombaiah, J.J. Vijaya, L.J. Kennedy, K. Kaviyarasu, *Mater. Chem. Phys.* **221**, 11 (2019)
7. W.E. Pottker, R. Ono, M.A. Cobos, A. Hernando, J.F.D.F. Araujo, A.C.O. Bruno, S.A. Lourenco, E. Longo, F.A.L. Porta, *Ceram. Int.* **44**, 17290 (2018)
8. Y. Pan, Y. Zhang, X. Wei, C. Yuan, J. Yin, D. Cao, G. Wang, *Electrochim. Acta* **109**, 89 (2013)
9. K.C.B. Naidu, W. Madhuri, *Mater. Chem. Phys.* **187**, 164 (2017)
10. Z.V. Mocanu, M. Airimioaei, C.E. Ciomaga, L. Curecheriu, F. Tudorache, S. Tascu, A.R. Iordan, N.N.M. Palamaru, L. Mitoseriu, *J. Mater. Sci.* **49**, 3276 (2014)

11. K.C.B. Naidu, S.R. Kiran, W. Madhuri, *Mater. Res. Bull.* **89**, 125 (2017)
12. T.A. Taha, A.A. Azab, M.A. Sebak, *J. Mol. Struct.* **1181**, 14 (2019)
13. M.A. Almessiere, Y. Slimani, S. Güner, A. Baykal, I. Ercan, *J. Rare Earths* **37**, 871 (2019)
14. S.V. Bhosale, P.S. Ekambe, S.V. Bhoraskar, V.L. Mathe, *Appl. Surf. Sci.* **441**, 724 (2018)
15. X.F. Wang, W. Ma, F. Jiang, E.S. Cao, K.M. Sun, L. Cheng, X.Z. Song, *Chem. Eng. J.* **338**, 504 (2018)
16. S. Zhang, W. Jiang, Y. Li, X. Yang, P. Sun, F. Liu, X. Yan, Y. Gao, X. Liang, J. Ma, G. Lu, *Sensors Actuators B Chem.* **291**, 266 (2019)
17. J. Jia, L. Qu, Z. Luo, Z. Wu, S. Jiang, X. Wu, B. Zhang, J. Xie, J. Li, J. Yang, *J. Environ. Chem. Eng.* **4**, 2865 (2016)
18. K. El-Sayed, M.B. Mohamed, S. Hamdy, S.S. Ata-Allah, *J. Magn. Magn. Mater.* **423**, 291 (2017)
19. M.Y. Rafique, M. Ellahi, M.Z. Iqbal, Q. Javed, L. Pan, *Mater. Lett.* **162**, 269 (2016)
20. F. Majid, J. Rauf, S. Ata, I. Bibi, A. Malik, S.M. Ibrahim, A. Ali, M. Iqbal, *Mater. Chem. Phys.* **258**, 123888 (2021)
21. M.M. Baig, E. Pervaiz, M. Azad, Z. Jahan, M.B.K. Niazi, S.M. Baig, *Ceram. Int.* **47**, 12557 (2021)
22. D. Mandal, A. Gorai, K. Mandal, *J. Magn. Magn. Mater.* **485**, 43 (2019)
23. D. Mandal, M. Alam, K. Mandal, *Phys. B Condens. Matter* **554**, 51 (2019)
24. B. Senthilkumar, R.K. Selvan, P. Vinothbabu, I. Perelshtein, A. Gedanken, *Mater. Chem. Phys.* **130**, 285 (2011)
25. S. Gao, G. Zhang, Y. Wang, X. Han, Y. Huang, P. Liu, *J. Mater. Sci. Tech.* **88**, 56 (2021)
26. R. Verma, A. Chauhan, K.M. Neha, R. Batoo, M. Kumar, M. Hadhi, E.H. Raslan, *Ceram. Int.* **47**, 3680 (2021)
27. M. Irfan, N. Dogan, A. Bingolbali, F. Aliew, *J. Magn. Magn. Mater.* **537**, 168150 (2021)
28. S. Dhaka, S. Kumar, K. Poonia, V. Singh, K. Dhaka, H.S. Mund, *J. Mater. Sci. Mater. Electron.* **32**, 16392 (2021)
29. P. Prajapat, S. Dhaka, H.S. Mund, *J. Elec. Mater.* **50**, 4671 (2021)
30. R.S. Yadav, J. Havlica, J. Masilko, L. Kalina, J. Wasserbauer, M. Hajdúchová, V. Enev, I. Kuřitka, Z. Kožáková, *J. Magn. Magn. Mater.* **394**, 439 (2015)
31. Z. Cvejic, E. Đurđić, G.I. Ivandekić, B. Bajac, P. Postolache, L. Mitoseriu, V.V. Srdic, S. Rakic, *J. Alloys Compd.* **649**, 1231 (2015)
32. A.R. Nitika, *Mater. Today Proceed.* **45**, 5444 (2021)
33. S.V. Bhandare, R. Kumar, A.V. Anupama, H.K. Choudhary, V.M. Jali, B. Sahoo, *Ceram. Int.* **46**, 17400 (2020)
34. N.A.S. Nogueira, V.H.S. Utuni, Y.C. Silva, P.K. Kiyohara, I.F. Vasconcelos, M.A.R. Miranda, J.M. Sasaki, *Mater. Chem. Phys.* **163**, 402 (2015)
35. T. Dippong, E.A. Levei, C. Leostean, O. Cadar, *J. Alloys Compd.* **868**, 159203 (2021)
36. G. Chandra, R.C. Srivastava, V.R. Reddy, H.M. Agrawal, *J. Magn. Magn. Mater.* **427**, 225 (2017)
37. M.A. Almessiere, Y. Slimani, B. Unal, T.I. Zubar, A. Sadaqat, A.V. Trukhanov, A. Baykal, *J. Mater. Res. Technol.* **9**, 10608 (2020)
38. J.H. Liu, L. Wang, F.S. Li, *J. Mater. Sci.* **40**, 2573 (2005)
39. S.K. Paswan, S. Kumari, M. Kar, A. Singh, H. Pathak, J.P. Borah, L. Kumar, *J. Phys. Chem. Solids* **151**, 109928 (2021)
40. A. Manikandan, J.J. Vijaya, L.J. Kennedy, M. Bououdina, *J. Mol. Struct.* **1035**, 332 (2013)
41. A. Loganathan, K. Kumar, *Appl. Nanosci.* **6**, 629 (2016)
42. M.A.S. Amulya, H.P. Nagaswarupa, M.R.A. Kumar, C.R. Ravikumar, S.C. Prashantha, K.B. Kusuma, *Appl. Surf. Sci. Adv.* **1**, 100023 (2020)
43. T. Tangcharoen, J.T. Thienprasert, C. Kongmark, *J. Adv. Ceram.* **8**, 352 (2019)
44. A.K.H. Bashir, N. Matinise, J. Sackey, K. Kaviyarasu, I.G. Madiba, L. Kodseti, F. Ezema, M. Maaza, *Physica E* **119**, 114002 (2020)
45. S. Joshi, M. Kumar, S. Chhoker, G. Srivastava, M. Jewariya, V.N. Singh, *J. Mol. Struct.* **1076**, 55 (2014)
46. S. Swathi, R. Yuvakkumar, P.S. Kumar, G. Ravi, D. Velauthapillai, *Chemosphere* **281**, 130903 (2021)
47. M.V. Ushakov, B. Senthilkumar, R. Kalai Selvan, I. Felner, M.I. Oshtrakh, *Mater. Chem. Phys.* **202**, 159 (2017)
48. A. Ahlawat, V.G. Sathe, V.R. Reddy, A. Gupta, *J. Magn. Magn. Mater.* **323**, 2049 (2011)
49. S.S. Shinde, S.S. Meena, S.M. Yusuf, K.Y. Rajpure, *J. Phys. Chem. C* **115**, 3731 (2011)
50. M. Hashim, S.S. Meena, R.K. Kotnala, S.E. Shirsath, A.S. Roy, A. Parveen, P. Bhatt, S. Kumar, R.B. Jotania, R. Kumar, *J. Alloys Compd.* **602**, 150 (2014)
51. A. Mitra, J. Mohapatra, S.S. Meena, C.V. Tomy, M. Aslam, *J. Phys. Chem. C* **118**, 19356 (2014)
52. H.N. Chaudhari, P.N. Dhruv, C. Singh, S.S. Meena, S. Kavita, R.B. Jotania, *J. Mater. Sci. Mater. Electron.* **31**, 18445 (2020)
53. K. Sharma, S. Singh, C.L. Prajapat, S. Bhattacharya, M.R. Jagannath, M.R. Singh, S.M. Yusuf, G.P. Kothiyal, *J. Magn. Magn. Mater.* **321**, 3821 (2009)
54. K. Sharma, Dixit, S. Singh, S. Jagannath, C.L. Bhattacharya, P.K. Prajapat, S.M. Sharma, A.K. Yusuf, A.K. Tyagi, G.P. Kothiyal, *J. Mater. Sci. and Eng. C* **29**, 2229 (2009)
55. K. Sharma, C.L. Prajapat, S.S. Meena, M.R. Singh, S.M. Yusuf, L. Montagne, G.P. Kothiyal, *J. Magn. Magn. Mater.* **345**, 24 (2013)

56. K. Sharma, S.S. Meena, S. Saxena, S.M. Yusuf, A. Srinivasan, G.P. Kothiyal, *Mater. Chem. Phys.* **133**, 144 (2012)
57. M. Hashim, S.S. Meena, R.K. Kotnala, S.E. Shirsath, P. Bhatt, S. Kumar, E. Şentürk, R. Kumar, N. Gupta, Alimuddin, *J. Magn. Magn. Mater.* **360**, 21 (2014)

**Publisher's Note** Springer Nature remains neutral with regard to jurisdictional claims in published maps and institutional affiliations.